Colloidal synthesis and characterization of monocrystalline apatite nanophosphors†

J. Y. Chane-Ching,*[a] A. Lebugle,[a] I. Rousselot,[a] A. Pourpoint[b] and F. Pellé[c]

DOI: 10.1039/b701194f

Here, we report the synthesis and characterization of 12 nm long, ultrafine, individualized calcium phosphate nanorods. Synthesis of these nanobuilding blocks involved the preparation of a calcium phosphate hybrid precursor containing an aminophosphate ligand. Colloidal calcium phosphate nanoparticles were achieved through the reorganization of an amorphous hybrid precursor at high temperature during a post-ageing step. These nanoparticles can be described as monocrystalline deficient calcium hydroxyapatite $Ca_{10-x}(PO_4)_{6-x}(HPO_4)_x(OH)_{2-x}$, with surfaces stabilized by $[PO_3^{2-}–O(CH_2)_2NH_3^+]$ groups. A model is proposed in which the [*ab*] plane of the nanoparticles is formed by 9 unit cells surrounded by a peripheral layer composed of twelve aminoethyl phosphate (AEP)-calcium phosphate ($xCa_9(PO_4)_6 - yCa\text{-}(AEP)_2$) hybrid units. Our ultrafine individualized calcium phosphate nanophosphors, synthesized in aqueous medium and displaying amino groups on their surface, are good candidates for use as fluorescent probes in biological imaging.

Introduction

There is intense scientific and technological interest in fabricating biological luminescent semiconductor nanocrystals as fluorescent biological labels for medical diagnostics and targeted therapeutics applications.[1–4] A variety of nanoparticles have been explored including CdSe, InP and InAs semiconductor nanocrystals. In comparison with conventional fluorophors, these nanocrystals have a narrow, tunable, symmetric emission spectrum. Since their absorbance onset and emission maximum shift to higher energy with decreasing size, variations of the material and variation of the size afford a spectral range of 400 nm to 2 μm in the peak emission. Nevertheless, many of the luminescent nanocrystals, *e.g.* the frequently used cadmium chalcogenides, are susceptible to photooxidation in the presence of water or oxygen.[5] Furthermore, since these nanocrystals contain Cd or As, the design and fabrication of less toxic luminescent nanocrystals are particularly attractive for broad and routine use in biology and medicine. An alternative class of nanomaterials to quantum dots would be achieved with nanophosphors as they could be excited under visible light illumination in order to avoid cell damage. In this context, Ln^{3+} doped calcium phosphate nanocrystals are good candidates and have been recently proposed.[6] The fine and well resolved emission lines provided by rare earth (RE) doped materials give an opportunity to realize multicolor biological probes. From the RE energy level schemes, it is possible to excite the different RE ions with a common excitation wavelength and to discriminate the different particles by their characteristic luminescence. Furthermore, RE ions can be efficiently excited in the visible range of the spectrum thus allowing experiments on living cells. The fluorescence is stable with time and does not exhibit "blinking behavior" as is observed in the case of quantum dots. The 4f–4f transitions are forbidden due to parity selection rules. The excited states therefore exhibit quite a long decay time (a few microseconds to a few milliseconds depending on the ion and the host) which easily allows suppression of the parasitic signal due to the autofluorescence of tissues. Among the rare earth ions, Eu^{3+} and Tb^{3+} are the best candidates since in these cases the main emitting state is separated from the lowest multiplets by several thousands of wavenumbers which precludes complete nonradiative de-excitation by multiphonon processes. Calcium phosphate could offer the advantages of being highly biocompatible, biodegradable,[7–10] stable in biological buffer solutions and easily conjugated to biomolecules through chemisorption due to the high affinity of calcium phosphate surfaces for proteins. Previous works have shown that finer spectral resolution in biological applications requires ultrafine particle sizes. Unfortunately, the above proposed synthetic routes reported in the literature yield aggregated bioapatite nanoparticles. In this context, individual apatite made of ultrafine unique crystallite need to be synthesized.

Various synthetic routes were recently proposed for the preparation of calcium phosphate nanoparticles displaying sizes ranging from 100 nm to 20 nm.[11] Control of particle size of aqueous colloids of hydroxyapatite nanoparticles has been recently described involving the presence of amino acids.[11] The amino acids ensured effective growth inhibition by adsorption of the amino acids predominantly onto the Ca rich surfaces

[a]*CIRIMAT, UMR 5085, CNRS, 118, Université Paul Sabatier, Route de Narbonne, 31062, Toulouse Cedex 9, France. E-mail: chane@chimie.ups-tlse.fr*
[b]*Rhodia Recherche et Technologie, 52 Rue de la Haie Coq, 93308, Aubervilliers Cedex, France*
[c]*LCAES, UMR 7574, Chimie de la Matière condensée de Paris, ENSCP, 11, Rue Pierre et Marie Curie, 75231, Paris Cedex, France*

during the initial stages of crystallization. These nanoparticles were formed by the oriented aggregation of primary crystallite domains along the *c* axis direction. The size of the domains was shown to be governed by the interactions with the amino acid additives which restrict the growth of the primary crystallites. Significant variations in the size of the nanoparticles were observed, consistent with the strength of binding at the HAP surfaces of a large range of amino acids, the smallest size L = 25 nm of the polycrystalline nanoparticles being observed with serine. Unfortunately, the proposed preparation route yields nanoparticles colloidally stabilized in basic pH, not suitable for biological applications. In order to minimize the influence of the luminescent nanocrystals on the biological mechanisms, the decrease of the size of the individual nanoparticles to the range of small proteins or oligonucleotides, *i.e.* <15 nm, will be desirable and will open up new opportunities as biological probes.

Here, we report the synthesis and characterization of aqueous monocrystalline calcium phosphate colloidal nanoparticles displaying sizes ~12 nm and colloidally stabilized in neutral pH. Our approach is based on the re-organisation induced by hydrothermal ageing at 80 °C of a hybrid precursor which contains aminoethyl phosphate (AEP) groups exhibiting strong complexation towards Ca^{2+}.[12–14] We have synthesized using our synthetic route Ln^{3+} (Ln^{3+} = Eu^{3+}, Tb^{3+}, *etc.*) doped calcium phosphate nanophosphors. These Ln^{3+} doped calcium phosphate nanophosphors display fluorescence under visible wavelength excitation from red to green and may be used in biological applications.

Experimental

Synthesis

Samples were prepared from reaction mixtures with the following molar composition: Ca : AEP : P_m = 3 : 3 : x, where P_m denotes the total mineral phosphate content (P_m = $H_3PO_4 + H_2PO_4^- + HPO_4^{2-} + PO_4^{3-}$). In a typical procedure, 0.112 g of CaO (2 mM Ca^{2+}) prepared from calcination of $CaCO_3$ at 950 °C was added in 15 min at room temperature to 25 ml of an aqueous 0.08 M solution of AEP (2 mM) while continuously stirring. Then, 4.7 ml of a 0.14 M H_3PO_4 solution (0.66 mM) was progressively added in 10 min to this suspension under stirring. We observed the formation of a white precipitate in the suspension. The resulting mixture was subsequently aged at 80 °C for 16 h. This led to a transparent colloidal dispersion (Scheme 1). Ln^{3+} doped calcium phosphate nanoparticles were prepared using the same procedure. Addition of 1 ml of a 0.2 M $Ln(NO_3)_3$ solution was performed under stirring in the acidic AEP solution. Pure calcium phosphate reference samples were prepared using the same procedure but without the incorporation of AEP. Ca-AEP and Ca-$(AEP)_2$ reference samples were prepared following a procedure previously described.[12]

Characterization

Detailed characterization of the solid precipitates of the non-aged suspensions, denoted solid precursors, was undertaken. These precursors were isolated by centrifugation (Discovery SE, Hitachi). Since the aged dispersions displayed colloidal stabilisation, colloidal particles were isolated by ultracentrifugation at 250 000 *g*. For precursors or isolated colloids, NMR was performed on the freshly prepared samples. Chemical analysis, FTIR and XRD were carried out on the solid after air drying at room temperature for four days. Studies on the aggregation state, size and morphology of individual apatite nanoparticles were undertaken by cryoTEM and TEM (JEOL 1200 EX, 120 keV). For cryoTEM, colloids were freeze-dried without any dilution with liquid ethane onto perforated membranes and transferred to a cooled sample holder maintained at liquid N_2 temperature. Mean particle dimensions were determined from high magnification TEM images of 50 randomly selected individual nanoparticles. Particle size was also verified as well as zeta potential determination using a Zetasizer 3000 Hsa (Malvern Instruments). After dissolution at room temperature of the precipitates in dilute acid, europium was determined by inductively coupled plasma atomic emission spectroscopy analysis (relative error 3%). Calcium and europium were assayed together by volumetric titration (relative error 0.5%). Orthophosphate ions were determined by colorimetry as phosphorus vanadomolybdate at λ = 460 nm with a relative error of 0.5%. The total phosphate concentration including orthophosphate and phosphate from AEP molecules was determined after treatment of the precipitates with perchloric acid at high temperature (200 °C). Solid state ^{31}P magic –angle spinning MAS NMR and ^{1}H MAS NMR spectra were recorded at 300 MHz on an AVANCE 300 Bruker spectrometer equipped with magic angle spinning CP-MAS probe and zirconium dioxide double bearing 4 mm rotors capable of spinning up to 10 kHz. The ^{1}H NMR spectra were recorded at 90°, with a 3 s relaxation time and 168 scans. A hydroxyapatite (HAP) sample was used as a secondary chemical shift reference in order to improve the chemical shift measurements. The ^{31}P NMR spectra were recorded at low angle ($\pi/8$) using a relaxation time of 120 s and 64 scans. Cross Polarisation (CP) from the protons together with proton decoupling was performed using mixing times of 1 ms, relaxation times of 5 s and 48 scans. XRD (CPS 120 INEL diffractometer using the $K_{\alpha 1}$ radiation of a cobalt anticathode (λ = 1.78892 Å)) and FTIR spectroscopy (Perkin Elmer FTIR

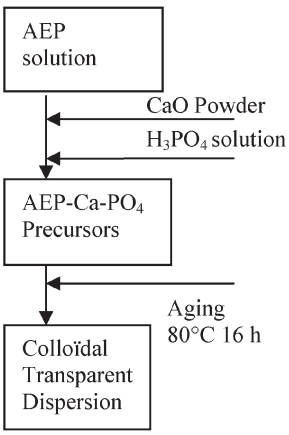

Scheme 1 Procedure for the preparation of monocrystalline colloidal apatite.

Table 1 $(AEP/Ca)_{mole}$ and $(P_m/Ca)_{mole}$ ratios determined in the dried, non aged precursors and aged colloids or precipitates

Starting mixture		Non aged sample		Aged sample	
(AEP/Ca)/mole	(P_m/Ca)/mole	(AEP/Ca)/mole	(P_m/Ca)/mole	(AEP/Ca)/mole	(P_m/Ca)/mole
1.00	0.083	0.32	0.51	0.165	0.56
1.00	0.166	0.28	0.57	0.14	0.60
1.00	0.250	0.26	0.58	0.14	0.60
1.00	0.333	0.22	0.60	0.14	0.60
1.00	0.416	0.19	0.59	0.14	0.58
1.00	0.500	0.19	0.62	0.125	0.60
1.00	0.666	0.12	0.68	0.10	0.65

1600 spectrometer) studies were performed on the dried powdered sample. Crystal domain sizes ($L_{(hkl)}$) along the *c* and *a* axes were calculated respectively from the (002) and (310) indexed XRD peaks, applying Scherrer's formula, $L_{(hkl)} = 0.94\lambda[\cos\theta\sqrt{(\Delta_r^2 - \Delta_o^2)}]^{-1}$, where θ is the diffraction angle for plane (*hkl*), Δ_r and Δ_o the widths in radians of reflection (*hkl*) at half height for the synthesized and HAP reference materials, respectively. A well crystallized reference sample was prepared by heating HAP at 900 °C for 72 h. The measurement accuracy from the (002) line was estimated as ± 0.5 nm, whereas the error for the (310) reflection was larger due to additional contributions from the (212) and (221) peaks.

For optical measurements, the colloidal suspensions were placed in quartz cells and the dried colloids were deposed on glass substrates. UV excitation was provided by the radiation of a mercury lamp and argon laser lines (Coherent Innova 90) were selected for excitation in the visible range of the spectrum. The fluorescence was dispersed by a HR460 Jobin-Yvon spectrometer, the signal analyzed by an ICCD-1024x256-18IRS Jobin-Yvon detector. For excitation spectra, the fluorescence was dispersed through a Jobin-Yvon HR1000 monochromator and the signal was sent to a RTC 56TVP photomultiplier tube (S20) and amplified by a lock-in amplifier (PAR 128A). The radiation from a xenon lamp (XBO 150) dispersed through a motorized double monochromator (Jobin-Yvon HD20) was used as excitation source. All spectra were corrected for the response of the detection set up.

Results and discussion

Our process involves the formation of a hybrid precursor from CaO, AEP and H_3PO_4 followed by an ageing step performed at 80 °C. Preliminary experiments have shown that successful preparation of colloidal building blocks requires both precise order of addition of the reactants and well determined AEP/Ca and P_m/Ca molar ratios. Colloidal dispersions were achieved with AEP/Ca $\geqslant$ 1 and P_m/Ca $\leqslant$ 0.33. These molar ratios correspond to theoretical conditions of full complexation of the PO_4^{3-} entities by Ca^{2+}, themselves interacting with AEP entities thus inhibiting the polycondensation of the calcium phosphate. We first present detailed characteristics of the non-aged precursors and then discuss the conditions for obtaining the colloidal nanophosphors.

Characteristics of the AEP-Ca-PO_4 precursors

XRD patterns recorded on precipitates synthesised with AEP/Ca = 1 and different mineral phosphate molar ratios (P_m/Ca = 0.083 to 0.66), centrifuged and dried at room temperature show a unique broad peak at $\theta = 16°$ indicating that the sample is X-ray amorphous.

Chemical compositions were determined for the various non-aged precipitates (Table 1). For a large range of Ca and P_m concentrations in the reaction mixture, $0.166 \leqslant P_m/Ca \leqslant 0.500$, a nearly constant P_m/Ca molar ratio in the non-aged precursor is observed. Incorporation of a significant amount of AEP in the non-aged precursors is experimentally achieved with decrease of the $(P_m/Ca)_{mole}$ ratio in the reacting mixture. An AEP/Ca maximum value (AEP/Ca = 0.32) much lower than the ratio incorporated in the reacting mixture (AEP/Ca = 1) is determined for the precipitates, probably due to the higher affinity of Ca^{2+} cation towards the mineral phosphate anion compared to AEP. Precursors synthesised at various (P_m/Ca) molar ratios, $(P_m/Ca)_{mole}$ = 0.66 and 0.33, were investigated by FTIR. First, we prepared various reference samples including pure calcium phosphate samples displaying various (P_m/Ca) molar ratios, and pure AEP, Ca-AEP and Ca-$(AEP)_2$ precipitates. In order to provide relevant information concerning peak assignments (see ESI†), we recorded FTIR spectra on all these reference samples. FTIR spectra recorded on the precursors synthesised at high (P_m/Ca) molar ratio, $(P_m/Ca)_{mole}$ = 0.66 (spectrum not shown here), display the typical vibrations usually mentioned for pure calcium phosphate reference samples. Although this spectrum corresponds to the precursor displaying a low concentration of AEP, we observe a peak due to the symmetric deformation of NH_3^+ at 1536 cm^{-1}[115,16] and a small peak attributed to the symmetric stretching of the P–O–C group, at 752.8 cm^{-1}.[17] This latter vibration, previously observed at 741 cm^{-1} in the $Ca(AEP)_2$ spectrum, is indeed slightly shifted suggesting close interaction of the AEP with amorphous calcium phosphate. Regarding the sample prepared at low (P_m/Ca) molar ratio, $(P_m/Ca)_{mole}$ = 0.33, peaks attributed to the CH vibration (1458 cm^{-1}) and NH_3^+ vibration (1536 cm^{-1}) are clearly observed suggesting higher concentration of AEP in the samples, consistent with the higher [AEP] concentration determined by chemical analysis. The large peak observed at 1383.3 cm^{-1} is attributed to the NO vibration of NO_3^- groups. The presence of NO_3^- impurity in the precursor arises from pH adjustment during the process involving HNO_3 addition. More important is the dissymmetric peak with a maximum at 543 cm^{-1} (Fig. 1) observed in the 700–500 cm^{-1} region, This peak appears significantly broad compared to the peak observed for reference samples prepared without AEP incorporation, and is similar to those usually observed on

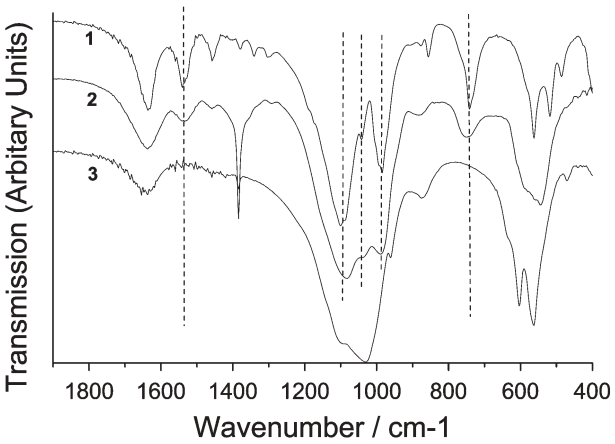

Fig. 1 FTIR spectra of 1) pure Ca-$(AEP)_2$ reference sample, 2) non-aged precursor synthesised at $(P_m/Ca)_{mole} = 0.33$, and 3) pure calcium phosphate reference sample. Comparison with pure calcium phosphate reference spectrum shows the amorphous character of the non-aged precursor.

amorphous calcium phosphate highlighting the amorphous character of the precursor. Decrease of the P_m concentration in the reacting mixture results in a drastic evolution of the strong PO_4^{3-} vibration bands over the region of 1000 cm^{-1}. The large band splits into three distinct bands observed at 989 cm^{-1}, 1040.3 cm^{-1} and 1084.7 cm^{-1}. These PO_4^{3-} peaks exhibit relative intensities similar to those determined for the reference Ca-$(AEP)_2$ sample. Nevertheless, in comparison to the Ca-$(AEP)_2$ spectrum, a small shift in the vibration frequencies is observed, probably resulting from close interactions with amorphous calcium phosphate. Indeed, a control experiment shows that this shift is not observed in the spectrum of the sample prepared by a physical mixture of $Ca(AEP)_2$ and amorphous calcium phosphate. All these observations suggest an intimate repartition of Ca-$(AEP)_2$ and amorphous calcium phosphate domains within the precursors. Thus, consistent with X-ray diffraction data, we observe by FTIR a significant evolution of the precursors with P_m concentration, more amorphous samples are synthesized at low P_m, $[P_m]/[Ca^{2+}] \leqslant 0.33$. A possible schematic representation of the precursors thus involves the presence of Ca-$(AEP)_2$ entities absorbed on amorphous $Ca_9(PO_4)_6$ clusters. As a reminder, these clusters, proposed by Betts and Posner,[18] are usually formed under conditions of high pH and large excess of Ca^{2+} towards PO_4^{3-}, similar conditions to those involved in the synthesis of our sample. From the chemical analysis data, we can determine an approximate ratio of one Ca-$(AEP)_2$ entity absorbed per $Ca_9(PO_4)_6$ cluster.

The local structure of the precipitates was also probed using ^1H NMR, single pulse and cross polarisation ^{31}P NMR. In order to facilitate assignment of the resonances found on our precipitates, ^1H and ^{31}P spectra were taken on pure AEP, Ca-AEP and Ca-$(AEP)_2$ precipitates. These ^1H and ^{31}P NMR reference data were completed by characterisation achieved on pure calcium phosphate reference samples prepared using the same procedure but without any addition of AEP. For the chemical shifts recorded on these reference samples, see ESI.† ^1H NMR spectra of the non-aged precursors exhibit sharp resonance lines at $\delta = 1.1$ ppm, $\delta = 3.6$ ppm and a very broad peak centred at $\delta = 6$ ppm. The peak at $\delta = 0$ ppm, usually assigned to the hydroxyapatite,[19,20] is not observed in these precursor spectra. The observed resonance peaks do not fit with ^1H NMR chemical shifts indexed for well known calcium phosphates structures such as hydroxyapatite, brushite or octacalcium phosphate.[19] Moreover, the observed chemical shift resonance peaks could not be attributed to Ca-AEP or Ca-$(AEP)_2$ complexes confirming that the precursors could not be considered as physical mixtures of these compounds with amorphous calcium phosphate. The decrease of the P_m/Ca ratio in the starting mixture, yielding to an increase of the AEP content in the precursors, gives rise to a significant increase of the intensity and the width of the broad peak. As previously reported by Yesinowski and Eckert,[19] the sharp peaks at $\delta = 1.1$ ppm, $\delta = 3.6$ ppm could arise from isolated structural water molecules undergoing rapid reorientation on the NMR scale. In contrast, the broad peak could be attributed to more mobile water species which are probably surface adsorbed. This assignment is consistent with the experimental observation of gel structures achieved on precursors prepared at low P_m/Ca ratios. For these latter samples, the high water content is probably due to the higher content of AEP protonated amine groups. A detailed ^{31}P NMR investigation was performed on the dried precursors prepared at $(AEP/Ca)_{mole} = 1$ and at various molar ratios ($(P_m/Ca) = 0.66$, 0.33 and 0.083). At low $[P_m]$, the chemical shift of the maximum ($\delta = 2.6$ ppm) is lower than the chemical shift determined for the pure Ca^{2+}–PO_4^{3-} reference samples ($\delta = 2.9$ ppm). In addition, the ^{31}P single pulse spectra for these samples exhibit a broad peak compared to reference samples prepared without AEP. The broadening of this peak is observed with the decrease of the P_m concentration in the reacting mixture (Fig. 2a). This broadening is correlated to a higher concentration of the AEP in the precursors as shown by the chemical analysis. A better insight of this broad peak is provided with the cross polarisation (CP) mode investigation. For the samples prepared at low $[P_m]$ concentration, $[P_m]/[Ca^{2+}] \leqslant 0.33$, a slight dissymmetry is observed in the region of lower chemical shift values (Fig. 2b). This dissymmetry involving the presence of various protonated

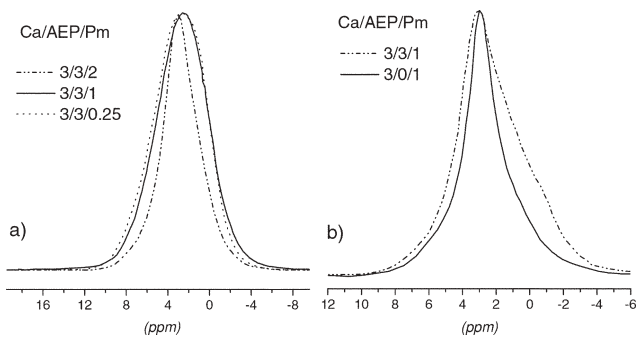

Fig. 2 a) Single pulse ^{31}P NMR spectra recorded on non-aged precursors prepared at various (P_m/Ca) molar ratios = 0.66, 0.33 and 0.08 showing a broadening of the peak when decreasing the P_m concentration in the reaction mixture. b) CP ^{31}P NMR spectrum of the (Ca:AEP:P_m = 3:3:1) non aged precursor showing the dissymmetry of the peak in the lower chemical shifts. Spectrum of a pure calcium phosphate sample (Ca : AEP : P_m = 3 : 0 : 1) is given for reference.

phosphate entities most likely arise from the presence of HPO_4^{2-} entities (δ = 1.4 ppm)[21] or protonated $Ca(AEP)_2$ entities (δ = −0.9 ppm). Moreover, a significant difference is observed between the chemical shifts of the maxima of the spectra recorded in single pulse mode and in cross polarisation mode, confirming that the observed broad peak in single pulse mode is indeed an envelope of several peaks.

We thus attempted to deconvolute the ^{31}P NMR single pulse peak recorded on the various precursors using the AEP, Ca-AEP, Ca-$(AEP)_2$ and Ca-PO_4 reference spectra. Unfortunately, our simulation does not provide an effective and unique analysis of the peak. Nevertheless, we suggest from our NMR investigation that the observed broadening and shift of the maximum to lower chemical shift values involve the various AEP, Ca-AEP, Ca-$(AEP)_2$ compounds in close interaction with an amorphous calcium phosphate. From the FTIR and NMR investigations performed on the non-aged samples, we highlight the hybrid character of the precursors composed of AEP, Ca-AEP entities and in a larger concentration, the presence of Ca-$(AEP)_2$ entities intimately associated with calcium phosphate. An increased hybrid character is observed on samples prepared from reacting mixtures possessing a low P_m concentration yielding an inhibition of calcium phosphate crystallisation and amorphous precursors. These hybrid precursors are characterised by a broad distribution of environments around the phosphorus atoms involving protonated phosphate entities.

Formation of calcium phosphate nanoparticles

The hydrothermal treatment at 80 °C of the precipitates within their reaction mixtures yields colloidal dispersions or precipitates depending on the initial composition of the reaction mixtures. White precipitates are formed after ageing at 80 °C for large $[P_m]/[Ca]$ ratios, *i.e.* $[P_m]/[Ca] \geqslant 0.66$. Decreasing the $[P_m]/[Ca]$ ratio results in the formation of opaque or transparent colloidal dispersions. Fully transparent colloidal dispersions are synthesised in a concentration domain delimited by $[P_m]/[Ca] \leqslant 0.33$ and $[AEP]/[Ca] \geqslant 0.80$. Continuous reorganisation during ageing of the solid phase synthesised at $[P_m]/[Ca] = 0.33$ and $[AEP]/[Ca] = 1.00$ was probed using chemical analysis, ^{31}P NMR and cryoTEM. After hydrothermal ageing, significant decrease of the [AEP]/[Ca] molar ratio is observed within the solid phase.

The colloidal nanoparticles prepared at $[P_m]/[Ca] = 0.33$ exhibit a [AEP]/[Ca] final molar ratio of 0.14 and those at $[P_m]/[Ca] = 0.6$ have a [AEP]/[Ca] similar to the molar ratio of hydroxyapatite. By varying the [AEP]/[Ca] ratio of the starting mixture in a wide range, an approximately constant [AEP]/[Ca] ratio is determined on the aged colloid. Thus, the successful preparation of colloidal transparent dispersions requires reorganisation operating from precursors displaying a high concentration of AEP. The ^{31}P single pulse NMR spectrum recorded after 1 h of thermal treatment exhibits a broad main peak at δ = 3.20 ppm. Further sharpening of this peak is observed with increasing ageing time (3 h). The peak sharpening could be attributed to either better crystallization or the formation of smaller domains and in both cases reveals a continuous reorganisation of the solid. This reorganisation is also evidenced by ^{1}H NMR showing the appearance of an OH resonance line at 0 ppm usually assigned to the OH group of hydroxyapatite, not observed in the non-aged precursors.

CryoTEM images of the dispersions before hydrothermal ageing show the presence of large bulky aggregates of micron size. In contrast, well defined individualised and monodisperse nanoparticles displaying anisotropic morphology are observed after the hydrothermal treatment suggesting a complete reorganisation of the solid (Fig. 3). To get a better insight into the mechanisms of formation of the colloidal nanoparticles, a control experiment prepared with similar composition but performed with delayed incorporation of AEP after addition of H_3PO_4 onto CaO slurry does not yield after hydrothermal treatment a transparent colloidal dispersion. Furthermore, another control experiment has shown the inability to obtain transparent colloidal dispersions of calcium phosphate when using preheated solutions of Ca^{2+}/AEP and HPO_4^{2-} at 80 °C before their co-addition into the reaction container. In contrast, another procedure yielding transparent colloidal dispersions displaying similar characteristics was successfully carried out using $CaCl_2$ or $Ca(NO_3)_2$ and $(NH_4)_2HPO_4$ solutions. In this procedure, a solid precursor is formed by reacting instantaneously at room temperature a Ca^{2+}/AEP solution with a HPO_4^{2-} solution followed by ageing at 80 °C. The pre-adjustment of the pH of the Ca^{2+} and HPO_4^{2-} solutions at pH 9 before mixing, required for obtaining transparent colloidal dispersions, suggests the formation of the colloidal nanoparticles operates from Ca^{2+}-PO_4^{3-}-AEP complexes. Moreover, the ageing temperature ranging from 60° to 100 °C is also of paramount importance since higher or lower temperatures yield non-colloidal dispersions or more aggregated dispersions. All these observations highlight that the formation of nanosized particles should require homogeneous [AEP] local distribution within the precursors prepared at room temperature, well defined supersaturation concentration and suggest decomplexation–rearrangement mechanisms occurring during the hydrothermal treatment of the hybrid precursor.

Characteristics of calcium phosphate nanoparticles

A detailed characterisation was then performed on colloidal calcium phosphate nanocrystals prepared at $[P_m]/[Ca] = 0.33$. CryoTEM images performed on the as-is dispersion without any dilution show perfectly individual nanoparticles (Fig. 3). TEM images performed at higher magnification indicate nanorod morphology of approximately 12 nm × 4 nm × 4 nm for the calcium phosphate nanoparticles. ^{31}P NMR spectra recorded on the freshly prepared ultracentrifuge aged samples exhibit a single broad peak centred at δ = 3.20 ppm. A continuous broadening of the peak is observed for decreasing values of $[P_m]/[Ca]$ from 0.66 to 0.08. For the colloids, this broadening can be attributed either to less crystallised colloids or to the finer dimensions of the particles.[20] A closer look at the ^{31}P NMR spectrum of the sample prepared at $[P_m]/[Ca] = 0.33$ shows a dissymmetric peak involving a second component with a chemical shift at 1.34 ppm, most likely due to the presence of HPO_4^- in the sample (Fig. 4).

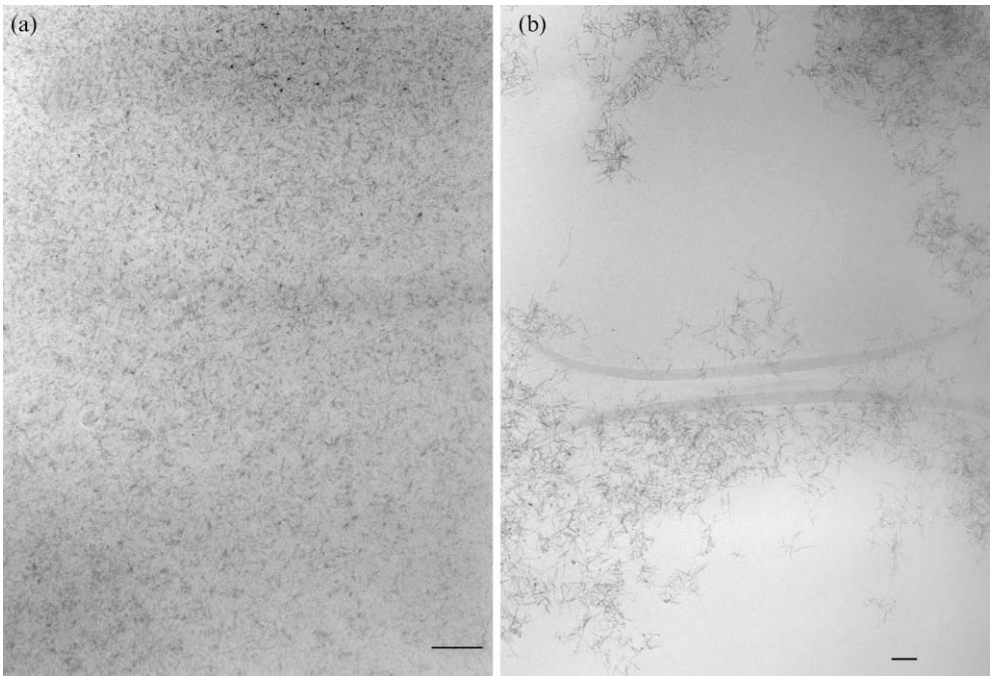

Fig. 3 a) CryoTEM of the colloidal calcium phosphate dispersion synthesised at $[P_m]/[Ca] = 0.33$ and $[AEP]/[Ca] = 1.00$ showing perfectly individualised nanoparticles; scale bar = 100 nm. b) TEM image showing nanorod morphology of around 12 nm length; scale bar = 20 nm.

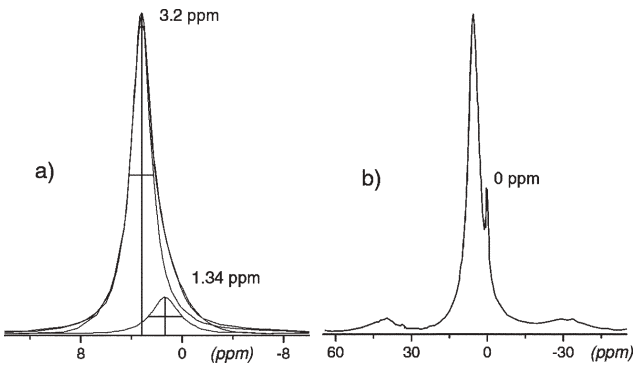

Fig. 4 NMR spectra recorded on aged and isolated colloids prepared at $[P_m]/[Ca] = 0.33$: a) deconvolution of the single pulse ^{31}P NMR showing a main peak at $\delta = 3.2$ ppm peak and a second at $\delta = 1.34$ ppm suggesting the presence of HPO_4^- in the product; b) ^1H NMR showing the presence of a peak centred at $\delta = 0$ ppm assigned to the OH group of hydroxyapatite.

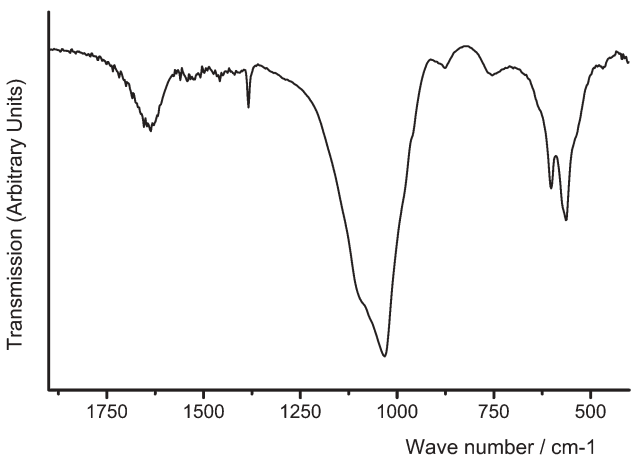

Fig. 5 FTIR spectrum of the (Ca : AEP : P_m = 3 : 3 : 1) dried colloids suggesting apatite structure of the colloids.

^1H NMR spectra recorded on the aged samples prepared at $[P_m]/[Ca] = 0.33$ show sharp resonance lines at $\delta = 0$ ppm, and a broad one centred at $\delta = 5.4$ ppm. The chemical shift at $\delta = 0$ ppm is assigned to the structural hydroxyl group and the broad peak centred at $\delta = 5.4$ ppm can be assigned to HPO_4^{2-} or surface-adsorbed water on hydroxyapatite.[19]

FTIR spectra recorded on dried colloids prepared at $[P_m]/[Ca] = 0.33$ and further isolated by ultracentrifuging (Fig. 5) display well defined peaks compared to the spectra recorded on the non-hydrothermal aged precursors. In the region 700–500 cm^{-1}, well defined peaks are observed at 602.1 cm^{-1} and 564.6 cm^{-1} and are assigned to the PO_4^{3-} v_4 vibration. These well defined peaks suggest that the nanoparticles exhibit some degree of crystallinity. However, the peak observed at 630 cm^{-1}, usually assigned to the OH vibration of hydroxyapatite, is poorly resolved. This is consistent with the NMR results showing the presence of HPO_4^{2-} in the structure and suggesting that the hydroxyapatite is indeed a deficient hydroxyapatite. In the region of 1000 cm^{-1}, we observed a broad peak resulting from an envelope of several peaks assigned to PO_4^{3-} stretching vibrational bands (v_1, v_3 vibrations) with a maximum at 1031 cm^{-1}. In comparison to the three distinct bands of the spectrum of the non-aged precursor, the envelope observed on the aged product, more representative of a pure apatite calcium phosphate, is consistent with the decrease of the AEP content as shown by chemical analysis. A peak is also observed at 875 cm^{-1}. This peak is usually attributed to the P–O vibration of the HPO_4^- group, consistent

with the NMR results. From these results, we suggest for the nanocrystals a calcium deficient hydroxyapatite structure. In addition, the presence of AEP in the dried colloids is confirmed by the peak observed at 755.6 cm^{-1}, assigned to a P–O–C vibration.

Zeta potential measurements show that unlike conventional HAP colloids, which are negatively charged at pH 8.5, AEP functionalized colloids are positively charged at this pH. We propose that the AEP molecules are bound to the nanocrystals surface through the Ca^{2+} complexation by the AEP phosphate groups. These aminoethyl phosphate molecules are most likely anchored to the nanoparticle surface through their phosphate groups with the rest of the molecule slightly tilted with respect to the surface. Due to these geometrical considerations, we assume, as proposed by Misra,[22] an effective area per PO_4^{3-} head group of 0.50 nm^2. A calculated ratio of [AEP]/[Ca] = 0.13 is then derived for monolayer coverage by the AEP molecules, using monocrystal dimensions of 12 nm × 4 nm × 4 nm, and a nanocrystal density value of 3. This value is close to the experimental value we have determined (0.14–0.16), confirming that the AEP molecules are bound on the nanocrystal surface. In contrast to the non-aged precursors spectra, the XRD pattern of the nanoparticles prepared at [AEP]/[Ca] = 1.00 and [P_m]/[Ca] = 0.33 (Fig. 6) clearly exhibits (002) and (310) peaks corresponding to an apatite structure. Using measurements of peak widths at half height for the (002) and (310) XRD reflections, crystal domain sizes of 12 nm and 4 nm were determined respectively along the crystallographic *c* and *a* axes. Since these values are similar to the values determined from cryoTEM observations, these nanoparticles could be described as monocrystalline nanocrystals. From all these observations, the nanoparticles could be identified as monocrystalline deficient calcium hydroxyapatite $Ca_{10-x}(PO_4)_{6-x}(HPO_4^-)_xOH_{2-x}$, with their surface stabilized by [PO_3^{2-}–$O(CH_2)_2NH_3^+$], charged AEP entities, the presence of HPO_4^- entities deriving from an internal hydrolysis of the PO_4^{3-} groups. As previously discussed, the formation of the colloidal nanocrystals involves rearrangement from PO_4^{3-}–Ca^{2+}–AEP hybrid precursors during the hydrothermal treatment. From the experimental sizes and chemical composition

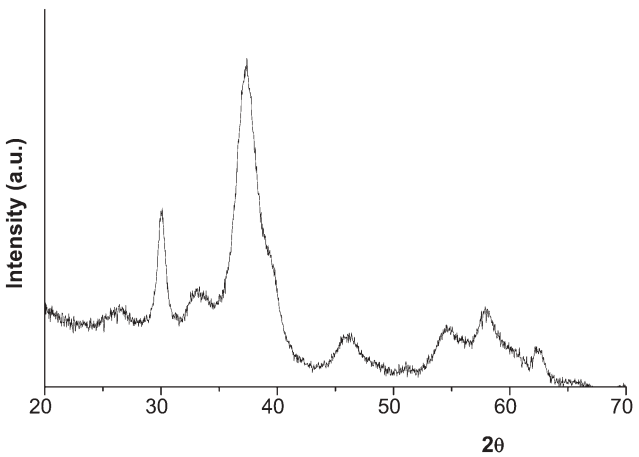

Fig. 6 XRD of the dried colloids prepared at (Ca : AEP : P_m) = (3 : 3 : 1) showing the apatite structure of the product.

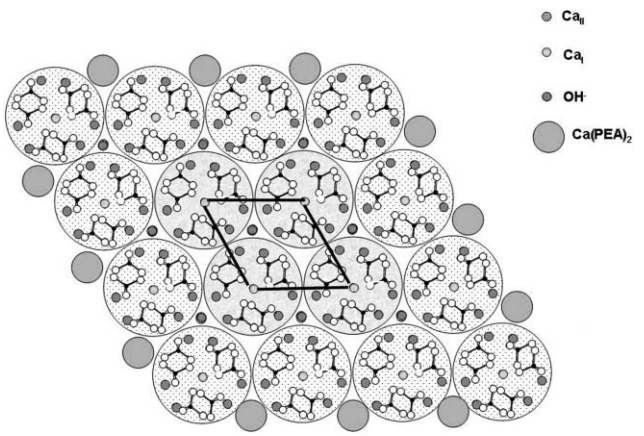

Fig. 7 Schematic representation of the calcium phosphate nanoparticles projected on the *ab* plane.

determined for these nanocrystals, we propose a schematic representation of the calcium phosphate nanocrystals structure, given in Fig. 7. From the experimental sizes determined in the [*ab*] plane of the nanocrystals, we propose a nanocrystal formed by 4 × 4 cell units. A possible mechanism describing the formation of these nanoparticles thus involves the condensation of four $Ca_9(PO_4)_6$ Posner clusters in a hexagonal structure, surrounded by a peripheral layer composed by twelve AEP–calcium phosphate ($xCa_9(PO_4)_6 - yCa$–$(AEP)_2$) hybrid units, inhibiting further growth of the crystal in the [*ab*] plane. The deficient hydroxyapatite structure results from the subsequent partial hydrolysis of PO_4^{3-} entities localized close to the so-formed tunnels in HPO_4^{2-} and OH^-. From all these observations, colloidal entities could be described as formed by $4Ca_9(PO_4)_5$–$(HPO_4)(OH)$ + $12Ca_9(PO_4)_6$, $Ca(AEP)_2$. This description is consistent with the results from chemical analysis performed on the isolated dried colloids. This schematic representation highlights that the inhibition of aggregation is along the *c* axis compared to nanocrystals prepared with the use of amino acid additives[11] and was achieved with better complexing of the Ca^{2+} localised in the 001 plane. Further decrease of the crystal size along the *c* axis should involve selection of additives displaying greater interactions with the Ca^{2+}. Preliminary results observed when reacting mixtures displaying AEP and P_m concentrations varying in a large range show a slight decrease of the crystal size along the *c* axis with decrease of the [P_m]/[Ca] ratio. At [AEP]/[Ca] = 1 and [P_m]/[Ca] = 0.083, XRD calculations provides a crystal domain size of around 8 nm. This smaller size along the *c* axis is accompanied by the formation of less crystallized nanocrystals although the 002 peak could still be clearly observed. Regarding this sample prepared at [P_m]/[Ca] = 0.083, the ^1H NMR pattern displays resonance lines at 0 ppm, 1.09 ppm, 3.63 ppm and a broad peak centred at 5.83 ppm. The very low intensity observed for the peak at δ = 0 ppm suggests that the decrease of crystallisation is accompanied by a significant modification of the structure of the nanocrystals. Further decrease of the nanocrystal size of these nanophosphors is currently under investigation using additives displaying greater interactions with Ca^{2+}. Preliminary experiments have

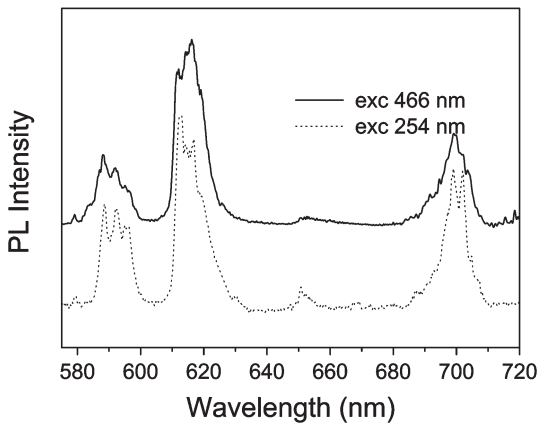

Fig. 8 Emission spectra of Eu^{3+} doped colloidal suspension under UV and visible excitation.

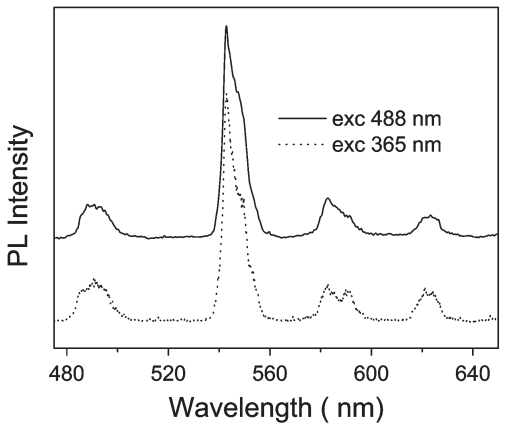

Fig. 9 Emission spectra of Tb^{3+} doped colloidal suspension under UV and visible excitation.

demonstrated the preparation of transparent colloidal dispersions using amino 2-ethylphosphonic acid.

Preparation and optical properties of Ln^{3+} doped calcium phosphate nanocrystals

Our synthetic procedure was applied to the synthesis of Ln^{3+} doped calcium phosphate nanophosphors. Various routes were examined for the incorporation of Ln^{3+} in calcium phosphate nanoparticles with the aim to avoid the undesirable formation of Ln_2O_3. Successful incorporation of Ln^{3+} doped nanoparticles ($Ln^{3+}/Ca^{2+} = 0.02$) was achieved with $Ln(NO_3)_3$ salt addition into the acidic AEP solution prior to increase the pH to 10 as a result of CaO addition. Upon ageing, transparent colloidal dispersions of Ln^{3+} ($Ln^{3+} = Eu^{3+}$, Tb^{3+}) were obtained for [AEP]/[Ca] = 1 and [P_m]/[Ca] = 0.33. CryoTEM observation of the colloids show individualised 12 nm length nanorods. The chemical analyses performed on the dried colloids isolated by ultracentrifugation indicate a molar composition (Ca : Ln^{3+} : AEP : P_m) = (1.617 : 0.033 : 0.24 : 1) yielding a molar ratio $Ln^{3+}/Ca^{2+} = 0.02$.

Emission spectra

Since these nanophosphors will be used in biological applications, their emission characteristics under UV excitation were compared to those obtained under visible excitation. The optical experiments performed on colloidal solutions and on dried colloids gave similar results.

Eu^{3+} doped nanoparticles. Under UV excitation, several spectral features were recorded between 570 and 720 nm which are easily ascribed to the 4f–4f transitions within the $4f^6$ configuration of Eu^{3+} ions, *i.e.* from the excited $^5D_0$ state to the lower ^7F_J multiplets (J = 0,1,2,3,4) (Fig. 8 and Table 2). Transitions from $^5D_0$ to $^7F_{5,6}$ are very weak and are not represented here. The emission spectrum is dominated by the forced electric dipole transitions $^5D_0 \rightarrow {}^7F_{2,4}$ observed at 617 and 698 nm respectively. The occurrence of electric dipole transitions (ED) with such intensity means that odd terms of the crystal field have important values since ED transitions can be observed due to the mixing of the 4f wavefunctions with those of opposite parity configurations. This allows one to conclude the absence of a center of symmetry for Eu^{3+} ions in the structure. Under visible excitation, emission spectra recorded for both samples are very similar to the previous ones. As an example, the $^5D_0 \rightarrow {}^7F_0$ (Eu^{3+}) transition has been fitted using a Gaussian lineshape, the calculated bandwidth from the UV excited spectrum (36.7 cm^{-1}) is the same as that obtained from the luminescence spectrum recorded with visible excitation (36.3 cm^{-1}). This result indicates that visible excitation is not selective and the inhomogeneous broadening is due to a slight disorder in the lattice and cannot be attributed to ions with different coordination numbers or occupying different crystallographic positions of the structure.

Tb^{3+} doped nanoparticles. The luminescence spectra of the colloidal suspension of terbium doped nanoparticles recorded with ultraviolet excitation are represented in Fig. 9. Several transitions are observed between 450 and 650 nm. According to the Tb^{3+} level scheme and previous papers,[23,24] the observed spectral features are assigned to emission from the $^5D_4$ excited state to the lowest multiplets ^7F_J (J = 6–3). As usual, the most efficient transition corresponds to the $^5D_4 \rightarrow {}^7F_5$ transition lying in the green range of the spectrum. No emission from the $^5D_3$ state could be recorded because of the quite high Tb^{3+} concentration which favors the depopulation of $^5D_3$ state by a

Table 2 Excitation and emission transitions observed for Ln^{3+} doped calcium phosphate nanophosphors

Ln^{3+}	Emission	Associated transition	Excitation	Associated transition
Eu^{3+}	614 nm	$^5D_0 \rightarrow {}^7F_2$	465 nm	$^7F_0 \rightarrow {}^5D_2$
	592 nm	$^5D_0 \rightarrow {}^7F_1$	396 nm	$^7F_0 \rightarrow {}^5L_6$
Tb^{3+}	489 nm	$^5D_4 \rightarrow {}^7F_6$	488 nm	$^7F_6 \rightarrow {}^5D_4$
	543 nm	$^5D_4 \rightarrow {}^7F_5$	369 nm	$^7F_6 \rightarrow {}^5D_3,{}^5G_6,{}^5L_{10}$
			352 nm	$^7F_6 \rightarrow {}^5G_5,{}^5D_2,{}^5G_4,{}^5L_9,{}^5G_3$

cross-relaxation process and/or by a multiphonon relaxation process to the $^5D_3$ multiplet; the probability of this non-radiative decay can be high due to the high phonon cutoff frequency of the host.

Excitation spectra

Eu^{3+} doped nanoparticles. In order to select the excitation wavelengths in the visible range suitable for our nanophosphors, the excitation spectrum of Eu^{3+} doped nanoparticles was recorded monitoring the hypersensitive $^5D_0 \rightarrow {}^7F_2$ transition. The spectrum extends from 540 to 220 nm (Fig. 10a) and the different excitation lines are ascribed to transitions from the $^7F_{0,1,2}$ to the excited states of the $4f^6(Eu^{3+})$ configuration since the $^7F_{1,2}$ multiplets are populated at room temperature. As shown in Fig. 10a, UV excitation in the $^5L_6$ state is the most efficient, however the energy of the $^5D_2$ state fits well with the argon laser line at 465.8 nm.

Tb^{3+} doped nanoparticles. The green luminescence of Tb^{3+} ion can be excited from the different upper levels as shown in the excitation spectrum performed monitoring the $^5D_4 \rightarrow {}^7F_5$ transition (Fig. 10b). Although the levels are closely spaced therefore difficult to identify individually, by comparison with other works, it is possible to assign groups of lines to several excited states. Even if the excitation efficiency in the $^5D_4$ multiplet is weak compared to that of the upper states, the energy is almost resonant with the argon laser line at 488 nm.

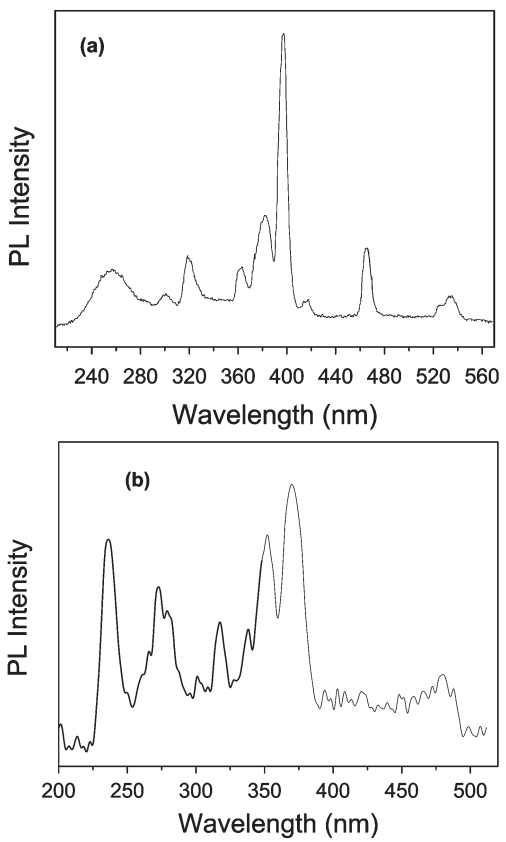

Fig. 10 Excitation spectra of RE^{3+} doped nanophosphors, recorded on the colloidal suspensions: a) $RE^{3+} = Eu^{3+}$, b) $RE^{3+} = Tb^{3+}$.

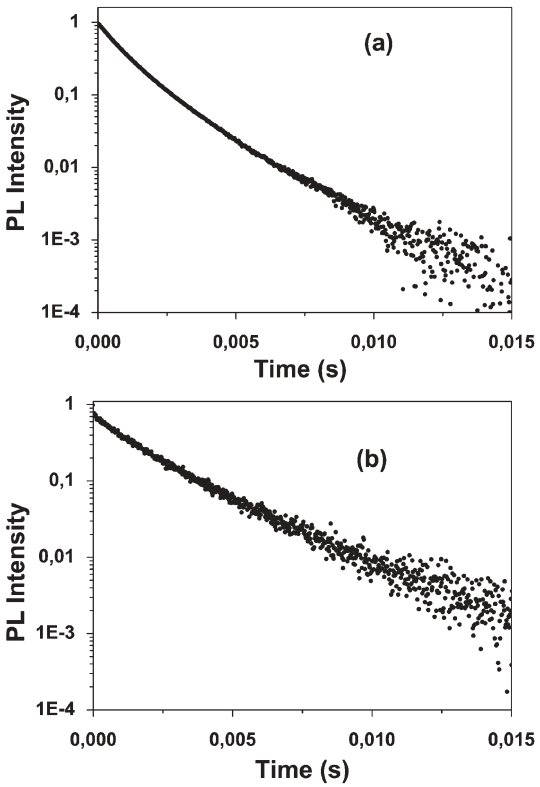

Fig. 11 Luminescence intensity *versus* time: a) $^5D_0$ (Eu^{3+}), b) $^5D_4$ (Tb^{3+}).

The main excitation and emission characteristics of the Ln^{3+} doped calcium phosphate colloidal nanoparticles are summarised in Table 2. Referring to Tb^{3+} doped nanoparticles, the excited levels are very close and cannot be separated at room temperature; their assignment is only given for multiplets observed at wavelengths lower than 350 nm.

Time resolved spectroscopy

The temporal transients of the emitting levels $^5D_0$ (Eu^{3+}) and $^5D_4$ (Tb^{3+}) have been measured at room temperature monitoring the red $^5D_0 \rightarrow {}^7F_2$ (Eu^{3+}) and green $^5D_4 \rightarrow {}^7F_5$ (Tb^{3+}) transitions respectively.

As shown in Fig. 11, the luminescence intensity does not follow a simple exponential function with decreasing time as is observed for small nanoparticles.[25,26] The long part of the decay can be fitted to an exponential function, the time constant was found to be equal to 1.4 ms and 2.2 ms for $^5D_0(Eu^{3+})$ and $^5D_4(Tb^{3+})$ respectively. The non-exponential behavior may be due to the presence of several emitting centers, the short lived species may be assigned to Ln^{3+} located on the surface and for which surface defects represent important non-radiative de-excitation pathways. Energy transfer between Ln^{3+} ions in aggregates can also explain the quenching of the emission. Further experiments are under way to identify the process responsible for the quenching. From our experiments, these results show that the fluorescence lifetime displayed by the nanophosphors is much longer than the autofluorescence of most proteins, increasing significantly the selectivity of the experiment.

Conclusions

Stable colloidal dispersions of individual monocrystalline hydroxyapatite nanocrystals were produced in the presence of aminoethyl phosphate (AEP). Individualised nanorods of hydroxyapatite were prepared from the ageing of hybrid precursors characterised by an intimate distribution of AEP, Ca-AEP and Ca-$(AEP)_2$ and amorphous calcium phosphate compounds as shown from NMR and FTIR investigations. The size of the nanoparticles is mainly influenced by the AEP/Ca molar ratio. The smallest crystal length of 12 nm was achieved from our preparation route involving de-complexation and rearrangement of the hybrid precursors. This procedure was applied to the preparation of luminescent calcium phosphate nanophosphors. Aqueous stable colloidal dispersions of luminescent Eu^{3+}, Tb^{3+} doped hydroxyapatite nanorods were synthesized, exhibiting a neutral pH. We demonstrated that these nanophosphors could display green and red emission peaks under excitation in the visible spectrum, allowing their use as fluorescent probes in biological applications. Compared to other quantum dots or other nanophosphors, calcium phosphate nanophosphors open new possibilities for use in biology due to their high biocompatibility, biodegradability and ease of derivatisation with biomolecules.

Acknowledgements

We thank Y. Klur for helpful discussions on NMR results and M. Airiau and A. Vacher for CryoTEM.

References

1 M. Bruchez, M. Moronne, P. Gin, S. Weiss and A. P. Alivisatos, *Science*, 1998, **281**, 2013.
2 X. Gao, W. C. W. Chan and S. Nie, *J. Biomed. Opt.*, 2002, **7**(4), 532.
3 J. Riegler and T. Nann, *Anal. Bioanal. Chem.*, 2004, **379**(7–8), 913.
4 X. Wu, H. Liu, K. N. Haley, J. A. Treadway, J. P. Larson, N. Ge, F. Peale and M. P. Bruchez, *Nat. Biotechnol.*, 2003, **21**, 41.
5 J. K. Jaiswal and S. M. Simon, *Trends Cell Biol.*, 2004, **14**(9), 497.
6 A. Doat, F. Pellé, N. Gardant and A. Lebugle, *J. Solid State Chem.*, 2004, **177**, 1179.
7 S. V. Dorozhktin and M. Epple, *Angew. Chem., Int. Ed.*, 2002, **41**, 3130.
8 Y. Kakizawa, S. Furukawa and K. Kataoaka, *J. Controlled Release*, 2004, **97**, 345.
9 J. L. Owens, H. S. Cheung and D. J. McCarty, *Calcif. Tissue Int.*, 1986, **38**, 170.
10 T. Welzel, I. Radtke, W. Meyer-Zaika, R. Heumann and M. Epple, *J. Mater. Chem.*, 2004, **14**, 2213.
11 R. Gonzalez-Mc Quire, J. Y. Chane-Ching, E. Vignaud, A. Lebugle and S. Mann, *J. Mater. Chem.*, 2004, **14**, 2277.
12 P. Bissinger, O. Kumberger and A. Schier, *Chem. Ber.*, 1991, **124**, 509.
13 M. S. Mohan and E. H. Abbott, *Inorg. Chem.*, 1978, **17**(8), 2203.
14 E. Zahidi, A. Lebugle and G. Bonel, *React. Solids*, 1985, 665.
15 B. Fowler, *Inorg. Chem.*, 1974, **13**, 194.
16 G. Socrates, *Infrared Characteristic Group Frequencies*, John Wiley and Sons, New York, 1994.
17 K. Nakamoto, *Infrared and Raman Spectra of Inorganic Coordination Compounds*, 4th edn, Wiley Interscience, NY, 1986.
18 F. Betts and A. S. Posner, *Trans. Am. Crystallogr. Assoc.*, 1974, **10**, 74.
19 P. J. Yesinowski and H. Eckert, *J. Am. Chem. Soc.*, 1987, **109**, 6274.
20 J. P. Yesinowski, *J. Am. Chem. Soc.*, 1981, **103**, 6266.
21 W. P. Rothwell, J. S. Waugh and J. P. Yesinowski, *J. Am. Chem. Soc.*, 1980, **102**(8), 2637.
22 D. N. Misra, *J. Colloid Interface Sci.*, 1997, **194**, 249.
23 N. Duhamel-Henry, J. L. Adam, B. Jacquier and C. Linarès, *Opt. Mater.*, 1996, **5**, 197.
24 G. Wakefield, H. A. Keron, P. J. Dobson and J. L. Hutchinson, *J. Phys. Chem. Solids*, 1999, **60**, 503.
25 D. K. Williams, H. Yuan and B. M. Tissue, *J. Lumin.*, 1999, **83–84**, 297.
26 W. Strek, E. Zych and D. Hreniak, *J. Alloys Compd.*, 2002, **344**, 332.